3D-CEUS tracking of injectable chemo-sonodynamic therapy-enabled mop-up of residual renal cell carcinoma after thermal ablation

Cuixian Li [a,b], Piao Zhu [d,**], Huijing Xiang [c], Yunjie Jin [a,b], Beilei Lu [a,b], Yujia Shen [a,b], Wenping Wang [a,b,***], Beijian Huang [a,b,****], Yu Chen [c,*]

[a] Department of Ultrasound, Zhongshan Hospital, Fudan University, Shanghai 200032, PR China
[b] Shanghai Institute of Medical Imaging, Fudan University, Shanghai 200032, PR China
[c] Materdicine Lab, School of Life Sciences, Shanghai University, Shanghai, 200444, PR China
[d] Shanghai Tenth People's Hospital, Shanghai Frontiers Science Center of Nanocatalytic Medicine, School of Medicine, Tongji University, Shanghai 200331, PR China

ARTICLE INFO

ABSTRACT

Thermal ablation (TA), as a minimally invasive therapeutic technique, has been extensively used to the treatment of solid tumors, such as renal cell carcinoma (RCC), which, unfortunately, still fails to overcome the high risk of local recurrence and distant metastasis since the incomplete ablation cannot be ignored due to various factors such as the indistinguishable tumor margins and limited ablation zone. Herein, we report the injectable thermosensitive hydrogel by confining curcumin (Cur)-loaded hollow mesoporous organosilica nanoparticles (Cur@HMON@gel) which can locate in tumor site more than half a month and mop up the residual RCC under ultrasound (US) irradiation after transforming from colloidal sol status to elastic gel matrix at physiological temperature. Based on the US-triggered accelerated diffusion of the model chemotherapy drug with multi-pharmacologic functions, the sustained and controlled release of Cur has been demonstrated *in vitro*. Significantly, US is employed as an external energy to trigger Cur, as a sonosensitizer also, to generate reactive oxygen species (ROS) for sonodynamic tumor therapy (SDT) in parallel. Tracking by the three-dimensional contrast-enhanced ultrasound (3D-CEUS) imaging, the typical decreased blood perfusions have been observed since the residual xenograft tumor after incomplete TA were effectively suppressed during the chemo-sonodynamic therapy process. The high *in vivo* biocompatibility and biodegradability of the multifunctional nanoplatform confined by thermogel provide the potential of their further clinical translation for the solid tumor eradication under the guidance and monitoring of 3D-CEUS.

1. Introduction

Renal cell carcinoma (RCC) is the most severe malignant tumor of kidney, and surgical resection is the conventional treatment for primary tumor [1,2]. With the development of the versatile imaging modalities, early diagnosis of small RCC is possible. Nevertheless, new alternative is urgently needed since a high proportion (20%–30%) of RCCs has already accompanied with distant metastasis in the first detection [3,4]. Thermal ablation (TA) is an emerging and minimally invasive therapeutic modality for solid neoplasm, which has been broadly applied in clinic for the treatment of various cancers [5,6]. However, by bringing benefits, TA also makes new challenges that the residual carcinoma holds high risk of accelerated recurrence or distant metastasis [7]. Typically, for multidrug-resistant advanced RCC, it doesn't make much sense to receive the conventional follow-up chemotherapy [8].Thus, new protocol to mopping up RCC after incomplete TA is eagerly awaited.

Alternatively, Curcumin (Cur), a natural xanthene dye with anti-inflammatory, antimicrobial, antitumor and other pharmacological activities, features therapeutic potential in a variety of cancers [9–11]. Furthermore, the photosensitive traits of Cur allow reactive oxygen species (ROS) generation upon light activation to augment the antitumor efficacy, which however suffers from poor penetration of the external light trigger into biological tissue [12–14]. Ultrasound (US), as an alternative external trigger with high tissue-penetrating depth and non-invasiveness [15–17], has been reported to activate some special sono-sensitizers with photosensitive traits (*e.g.* Cur) to generate toxic ROS for therapeutics, named as sonodynamic therapy (SDT) [18,19]. Unfortunately, the low bioavailability and biological/chemical instability of the chemo-sonodynamic therapeutic agent Cur hinder its clinical translation [20,21].

Retrospectively, remarkable progresses have been made to improve the bioavailability by incorporating Cur into polymeric nanoparticles, amino acid conjugates or liposomes [22–25]. These organic therapeutic systems result in unavoidable leakage before reaching the desired tissues or burst release upon external triggering because of the instability in biological environment. Hollow mesoporous organosilica nanoparticle (HMON) has inspired intensive interest in drug delivery due to the high drug-loading capacity, ingenious adjustable composition, and rich surface chemical functions [55,56], which has been highlighted to be biocompatible and stable in physiological system. Hydrophobic drug encapsulated in HMON shows a sustained low-dose release pattern in target tissue [26–28], which is favorable for the treatment of chronic diseases such as diabetes or hypertension [29,30]. However, as for malignant tumors, the long-term and continuous exposure to low-level administration will lead to drug tolerance and fail to tumor growth suppression [31,32]. Fortunately, the on-demand and controlled release of the drug encapsulated in HMON can be achieved upon US triggering [33,34]. In this work, physiologically active tetrasulfide bond was adopted to fabricate organic-inorganic hybrid nanocarriers, which have been demonstrated to be specifically biodegradable in tumor microenvironment (TME) with high concentration of glutathione (GSH) [35,36]. After loading Cur (Cur@HMON), an injectable thermosensitive hydrogel was designed to confine the Cur@HMON (Cur@HMON@gel) in tumor region *via* phase transformation at body temperature. The biodegradation of thermogel has been systematically evaluated both *in vitro* at liquid level and *in vivo* on tumor-bearing mice. Additionally, the Cur@HMON@gel located in tumor site can function for at least half a month after a single injection, consequently avoiding the repeated administration of anti-tumor agents. Upon US triggering, the residual RCC after incomplete TA, incomplete laser ablation (ILA) in this work, was mopped up by the local release of Cur accompanying with the generation of ROS.

For tracking this chemo-sonodynamic therapy process, three-dimensional contrast-enhanced ultrasound (3D-CEUS), an objective, simple and reproducible technique for real time imaging, was chosen to display the dynamic perfusion of the whole tumor rather than traditional *in vivo* fluorescence imaging or tumor volume calculation based on the measured diameter of subcutaneous tumor that could be easily influenced by artificial factors [37,38]. Especially and importantly, tumors in the early stage of non-surgical treatment, such as TA and targeted therapy, are usually characterized by decreased blood supply or intra-tumor necrosis, rather than tumor volume reduction [39,40]. Especially, this work provides the first paradigm for rescuing the incomplete TA *via* chemo/sonodynamic synergistic therapy by a multifunctional biomaterial platform, and demonstrates the potential for therapeutic monitoring and guidance during non-surgical treatment.

2. Experimental section

2.1. Materials

All reagents were of analytical grade and used without any purification. Tetraethoxysilane (TEOS), ammonia solution (NH₃·H₂O) (25%–28%), methanol, acetic acid anhydrous and anhydrous ethanol were purchased from Sinopharm Chemical Reagent Co., Ltd. Triethanolamine (TEA), bis[3-(triethoxysilyl)propyl]tetrasulfide (BTES), Chitosan (CS) and β-glycerophosphate (β-GP) were obtained from Aladdin Co., Ltd. Cetyltrimethylammonium chloride (CTAC), Sodium chloride (NaCl), Fluorescein isothiocyanate (FITC) and curcumin (Cur) were purchased from Sigma-Aldrich Co., Ltd. Dimethyl sulfoxide (DMSO), Annexin V, FITC Apoptosis Detection Kit, Calcein-AM/PI Double Staining Kit and Cell Counting Kit-8 (CCK-8) were obtained from Dojindo Chemical technology Co., ltd. 2',7'-dichlorofluorescein diacetate (DCFH-DA), 4',6-diamidino-2-phenylindole (DAPI) were purchased from Beyotime Institute of Biotechnology, Shanghai, China. Singlet Oxygen Sensor Green (SOSG, Invitrogen Co., Ltd.) probe and methoxy poly (ethylene glycol) silane (mPEG, Jenkem Technology Co., Ltd.) were purchased from Shanghai Yare Biotechnology Co., Ltd, Shanghai. Deionized water was used in all experiments. All chemicals were used as received without further purification.

2.2. Synthesis of Cur@HMON@gel

a. Synthesis of (HMON)

HMON was obtained based on a well-established structural difference-based alkaline etching strategy. Typically, a CTAC aqueous solution (10 g, 10 wt%) and a TEA aqueous solution (0.4 g, 10 wt%) were mixed and stirred at room temperature for 30 min, followed by the addition of 0.75 mL TEOS dropwise in a 95 °C water bath with the magnetic stirring speed of 300 rpm. The mesoporous silica nanoparticle (MSN) was formed after hydrolysis/condensation reaction for 1 h, and the mixture of BTES (1 mL) and TEOS (0.5 mL) were then added to the system and stirred for another 4 h. After being washed with ethanol three times, the resultant MSN@MON particles and 4 mL of NH₃·H₂O were dispersed in 210 mL of deionized water and reacted for additional 3 h at 95 °C water bath. The product HMON was collected by centrifugation and washed with water three times. To remove CTAC in particles, the as-synthesized HMON was extracted in methanol (400 mL) with NaCl (5 g) by magnetic stirring for 3 times (each time for 12 h).

b. Synthesis of Cur@HMON

The obtained HMON ethanol dispersion was added to Cur solution (1 mg·mL⁻¹ in ethanol, 10 mL) under magnetic stirring in the dark for 24 h, and the mixtures were centrifuged and washed with ethanol for three times to remove residual Cur, the supernatant was collected for further calculating of loading capacity. Ultraviolet absorption spectrum of gradient concentration of Cur from 200 to 700 nm were obtained by dissolving Cur in phosphate-buffered saline (PBS) containing 1% (v/v) DMSO, and the corresponding standard curve between Cur weight and UV absorbance at 425 nm was calculated. The dosage of Cur in the above supernatant was calculated and the drug encapsulation efficiency of HMON was derived according to the following equation:

$$\text{Drug Encapsulation Efficiency}(\%) = \frac{\text{Total Cur} - \text{Cur in supernatant}}{\text{Total Cur}} \times 100 \tag{1}$$

$$\text{Drug Loading Capacity}(\%) = \frac{\text{Cur in Cur@HMON}}{\text{Total weight of Cur@HMON}} \times 100 \tag{2}$$

c. Synthesis of Cur@HMON@gel

The hydrogel was prepared using a previous method with slightly modifications [55,56]. Briefly, CS solution was firstly obtained by dissolving CS powder (100 mg) in hydrochloric acid (HCl, 0.1 M, 4 mL) and stirred at room temperature until the solution was clear, and 500 mgβ-GP

was dissolved in 1 mL of deionized water. The two solutions were cooled to 4 °C and then β-GP was added into CS solution dropwise under mild agitation. The resultant CS/β-GP hydrogel (gel) (5 mL, containing 2% (w/v) CS and 10% (w/v) β-GP, pH = 7.2) was mixed with Cur@HMON (200 mg) and magnetic stirred at 4 °C for 12 h, by which Cur@HMON@gel was synthesized and then stored at 4 °C for further application.

2.3. Characterization

The dynamic light scattering (DLS) measurement and the zeta potential of nanoparticles were determined using a Zetasizer Nanoseries (Nano ZS90, Malvern Instrument Ltd., UK). The morphology and the structure of nanoparticles were observed by scanning electron microscopy (SEM, Magellan 400, FEI Company, US) and transmission electron microscopy (TEM, JEM-2100F, JEOL, Japan). UV–Vis–NIR absorption spectra were recorded by a UV–Vis–NIR spectrometer (UV-3600, Shimadzu, Japan) with QS-grade quartz cuvettes at room temperature. The confocal laser scanning microscopy (CLSM) photographs were acquired in FV1000 (Olympus Company, Japan). Flow cytometry analysis for cell apoptosis were conducted by BD LSRFortessa. The element quantified analysis of sample was performed on inductively coupled plasma-optical emission spectrometry (ICP-OES, Agilent 725, Agilent Technologies, US). The element quantitative analysis of sample was conducted on inductively coupled plasma-optical emission spectrometry (ICP-OES, Agilent 725, Agilent Technologies, US). The rheological properties of CS/β-GP hydrogel were explored using a rotational rheometer (Physica MCR 301, Anton Paar instrument, Germany). The evolution of the storage (G') and loss (G'') moduli was determined at a constant shear stress of 1 Pa and at a fixed frequency of 1 Hz. The Electron spin resonance (ESR) characterization was performed on a Bruker EMX electron paramagnetic resonance spectrometer. And all ultrasound experiments with low power density were conducted on a portable ultrasound apparatus (Sonicator 740, Mettler Electronics, US).

2.4. Sol-gel transitions of CS/β-GP hydrogels

A series of hydrogels composed of 2% (w/v) CS and vary ratios of β-GP (5%, 10% and 15%, w/v), denoted as CS (2%)/β-GP (5%), CS (2%)/β-GP (10%) and CS (2%)/β-GP (15%) thermogels respectively, were prepared following the procedure described above. The sol-gel transition temperature was determined by the method of vial-inverting method. Briefly, 5 mL of hydrogel was transferred into a 20 mL vial and soaked in water bath with the certain temperature for 10 min. The temperature of water bath was varied from 20 °C to 50 °C with an increment of 1 °C per time. When no visual flow can be observed within 1 min, the hydrogel was considered to be elastic gel phase, and the temperature was defined as the transition temperature of hydrogel. In addition, the sol-gel transition duration of these hydrogels at 37 °C was observed using the same method with a time interval of 1 min. Based on the above results, the thermal hydrogel whose gelation temperature is approaching body temperature was selected for further rheological tests. The time- and temperature-dependent storage modulus (G') and loss modulus (G'') of hydrogel were measured in the linear viscoelastic region at a constant shear. The evaluation duration was 2000 s at physiological temperature (37 °C). And the transition temperature was conducted under the increasing temperature from 20 to 50 °C with constant heating rate of 1 °C per minute. The phase transition time and temperature were obtained at the intersection point of G' and G''.

2.5. Water absorption capability of hydrogel

In order to evaluate the cross-linking density and drug-loading potential of the hydrogels prepared above, their water absorption capacity closely related to the pore size of hydrogel and entanglement strength

between the chains was calculated. Three freeze-dried hydrogel samples were weighed and immersed in 50 mL of PBS at 37 °C and neutral pH. The samples were taken out, dried surface with filter paper and weighted every 20 min, the process was repeated until the constant weight was attained. Water absorption capability of hydrogel was measured by the following equation.

$$\text{Water Absorption (WA)} = \frac{W_2 - W_1}{W_1} \times 100\% \tag{3}$$

where W_1 represents the weight of dry hydrogels and W_2 represents the weight of water absorbed hydrogels.

2.6. In vitro evaluation of hydrogel degradation

To explore the degradation property of hydrogel, 4 mL of gel was transferred into a 20 mL vial with 15 mL of simulated body fluid (pH = 7.4) and saved at 37 °C. The morphology of the hydrogel was recorded and the simulated body fluid was refreshed every 5 days until 45 days.

After embedding Cur@HMON into the hydrogel matrix, the degradation behavior was also observed for 30 days. Cur@HMON@gel was weighted every 5 days and degradation performance was quantitative analyzed by the following equation.

$$\text{Hydrogel Degradation (HD)} = \frac{W1 - W2}{W_1} \times 100\% \tag{4}$$

where W_1 represents the initial weight of swelled Cur@HMON@gel and W_2 represents the weight of remained Cur@HMON@gel.

2.7. In vitro drug release upon ultrasound (US) triggering

The *in vitro* Cur releasing behavior was evaluated by a modified dialysis method. In detail, 1 mL for each of the 6 samples (Cur, Cur@HMON, Cur@gel, and Cur@HMON@gel × 2, all with 1 mg mL^{-1} of Cur), were placed in dialysis bags (molecular mass cut-off was 3.5 kDa) and then immersed into a 50 mL test tube, in which 40 mL of PBS (pH 7.4, 37 °C) containing 1% DMSO (v/v) was added. To investigate drug release kinetics under US irradiation, one sample of Cur@gel and Cur@HMON@gel were selected for ultrasonic irradiation (1.5 W·cm^{-2}, 1 MHz, with 50% duty cycle) for six cycles. And the Cur, Cur@HMON Cur@gel and Cur@HMON@gel group with no stimulus were conducted to compare the spontaneous drug release of different drug delivery system. The tubes were placed in an orbital shaker (100 rpm). At each interval of 1 h, 3 mL of release medium was collected for UV detector at 425 nm and then returned to original tubes.

2.8. Evidence of reactive oxygen species (ROS) generation in vitro

To verify the sonodynamic potential of Cur and Cur@HMON@gel, SOSG was employed as a chemical probe for ROS as it is highly selective for singlet oxygen ($^1O_2$). Briefly, the stock solution was prepared by dissolving 100 μg of SOSG in 330 μL of methanol, 30 μL of stock solution was then added to 5970 μL of PBS containing Cur (10 μg·mL^{-1} in terminal solution). The fluorescence intensity of work solution received no US irritation was saved as the reference line, and US (1.5 W·cm^{-2}, 1 MHz, 50% duty cycle, 1 min) was applied with 1 min intervals and the fluorescence intensity of work solution was recorded immediately (excitation/emission wave length: 488/525 nm).

Electron spin resonance (ESR) spectroscopy was applied to further detect $^1O_2$ generated by US + Cur@HMON@gel, and 2, 2, 6, 6-tetramethylpiperidine (TEMP) was adopted as a spin-trapping agent to visualize the signal of $^1O_2$ production. Generally, Cur@HMON@gel with Cur of 10 μg·mL^{-1} was exposed to US irradiation (1.5 W·cm^{-2}, 1.0 MHz, 50% duty cycle) for 1 min in the presence of TEMP (97 μM). The $^1O_2$ signal was immediately detected by the ESR spectrometer. In addition, the

Cur@HMON@gel + TEMP group, US + Cur + TEMP group, Cur + TEMP group, US + TEMP group and TEMP group were also tested for comparison.

2.9. Cell experiments

a. Cell culture

HUVECs (human umbilical vein endothelial cells, bought from Cell Bank of Shanghai Institutes for Biological Sciences, Chinese Academy of Sciences) were maintained in DMEM medium, and 786-O cancer cells (the cell line from human clear cell renal cell carcinoma , obtained from the American Tissue Culture Collection) were cultured in RPMI-1640 medium (Hyclone), all medium were supplemented with 1% penicillin-streptomycin (Gibco) and 10% fetal bovine serum (Gibco). Cells were maintained at 37 °C with 5% CO_2 in cell culture incubator (Thermo Fisher Scientific).

b. Detection of intracellular ROS generation

786-O cells ($1 \times 10^5 \cdot well^{-1}$) were seeded in CLSM-exclusive culture dishes and allowed to adhere for 12 h. The culture medium was substituted by fresh medium containing Cur (10 μg·mL^{-1}), Cur@HMON@gel (bearing Cur concentration of 10 μg·mL^{-1}) or pure culture medium and then incubated for another 4 h. The cell medium was substituted by 1 mL of FBS-free medium containing DCFH-DA (10 μM) and incubated for 20 min. For the positive control group, cells were incubated with Rosup reagent for 30 min. After been washed with PBS for three times and replaced DCFH-DA solution with complete cell medium, half number of each kind of wells were selected for ultrasonic irradiation (1 MHz, 1.5 W·cm^{-2}, 50% duty cycle, 1 min). Nuclei were counterstained with DAPI for 15 min, washed with PBS for two times and then visualized *via* confocal laser scanning microscopy (CLSM) with 405 nm and 488 nm excitation wavelength. The fluorescence intensity generated by ROS was quantitatively evaluated by image analysis software Image J (National Institutes of Health, USA).

c. Cytotoxicity evaluation

A standard CCK-8 viability assay was used for cytotoxicity assessment of Cur and Cur@HMON@gel. HUVECs and 786-O cells were seeded in lower chamber of the 24-well transwell system (Corning Co., Ltd., US) with density of 1×10^4 cells per well and incubated for 24 h. For Cur@HMON@gel group, hydrogels containing a gradient concentration of Cur (0, 0.15625, 0.3125, 0.625, 1.25, 2.5, 5, 10, 20 and 40 μg·mL^{-1}) were dropped on the upper chamber and incubated 10 min at 37 °C. After the hydrogel transform into gel state, the upper chamber was transferred to the cell-seeded plates and 200 μL of culture medium was added. For Cur groups, the culture medium containing Cur was added into the upper chamber directly to achieve the same terminal gradient concentration (0, 0.15625, 0.3125, 0.625, 1.25, 2.5, 5, 10, 20 and 40 μg·mL^{-1}) as those of Cur@HMON@gel group. After another 24 h co-incubation, the upper chambers were removed and the viabilities of cell were evaluated by CCK-8 assays. In consideration of the application of the DMSO in all cell-line assessment for Cur dissolving due to its poor water solubility. The cytotoxicity of DMSO (0, 0.083125, 0.16625, 0.3125, 0.625, 1.25, 2.5, 5, 10 and 20%, v/v%) to HUVECs and 786-O cell lines were also evaluated. Each data point was measured for nine times.

For further measure the sonotoxicity of different nanosystems under US, the additional experiments were administrated to obtain the 786-O cells viability with or without US irradiation. The cell culture was carried out according the above methods and then co-incubated with different culture mediums (untreated cells as control, Cur, HMON, blank gel, Cur@gel and Cur@HMON@gel groups, with Cur concentration of 10 μg·mL^{-1}) for 12 h. For all US irradiation groups, the same US protocol was applied (1.5 W·cm^{-2}, 1 MHz, 50% cycle, 1.5 min), after that, the

following another 4 h co-incubated was performed and the cells were wash with PBS three times for all groups, the standard CCK-8 assays were used to evaluated cell viabilities of different groups.

After that, flow cytometry analysis and CLSM observation were applied to verify the apoptosis of cells, and the procedure was similar to the ROS detection as mentioned above except replace DCFH-DA with Annexin V-FITC/PI and Calcein-AM/PI, followed by measurement with BD LSRFortessa and CLSM, respectively.

With the purpose of exploring the influence of different treatment parameters on sonotoxicity to RCC cells, the cell viabilities of 786-O cells under different US power density (0, 0.5, 0.8, 1, 1.5 and 2.0 W·cm^{-2}), US irradiation duration (0, 0.5, 1, 2, 3 and 4 min) and varied Cur concentration (0, 0.625, 1.25, 2.5, 5 and 10 μg·mL^{-1}) were obtained by standard CCK-8 assays using the same procedures as sonotoxicity evaluation of different nanosystem mentioned above.

2.10. In vivo experiments

a. Animals

All procedures on laboratory animals were complied with the guidelines of the Institute of Animal Care and Use Committee of Zhongshan Hospital, Fudan University (IACUC, No. 2020–073). Male BALB/c nude mice with an average age of 5 weeks (18–20 g) were purchased from Shanghai Institute of Material Medicine and used for the establishment of RCC subcutaneous xenograft and the corresponding assessments of antitumor efficiency of Cur@HMON@gel and US. Male Kunming mice with an average age of 4 weeks (20 ± 2 g) were used to evaluate the biocompatibility of Cur@HMON@gel and the degradation of hydrogel *in vivo*. All mice were maintained in specific pathogen-free (SPF) conditions during the experience procedures.

b. In vivo biocompatibility assay and degradation of hydrogel

Kunming mice (n = 15) were divided into control group (the group accepted 100 μL of PBS injection, n = 3) and hydrogel group (n = 12), and 100 μL of CS/β-GP hydrogel solution was injected into the right flank of Kunming mice. The body weight of mice was recorded every 3 days. At particular time points (1 month for control group; 30 min, 1 week, 2 weeks and 1 month for hydrogel group), three mice of each groups were sacrificed to observe the gel state, and the skin tissues adjacent to hydrogel and the main organs (heart, liver, spleen, lung and kidney) were harvested for biocompatibility evaluation by hematoxylin and eosin (H&E) staining.

c. In vivo chemo-sonodynamic therapy in eliminating residual tumor after incomplete laser ablation (ILA)

The therapeutic efficacy of US irradiated Cur@HMON@gel nanosystem was assessed in subcutaneous 786-O tumor-bearing mice. Approximate 5×10^6 786–0 cells were subcutaneously injected into right flanks of 60 nude mice to establish subcutaneous xenograft model. The size of tumors was regularly measured every three days using a high-frequency linear array ultrasonic probe (L18-5, Aplio500, central frequency is 12 MHz, range 7–18 MHz; Toshiba Medical Systems Corporation, Tochigi, Japan) until it reached 8 mm in maximal diameter. The tumor bearing mice were randomly assigned to the following six groups (n = 10): control (no treatment was given), ILA (1064 nm ± 10 nm, 3.0 W, 10 s), ILA + Cur (1 mg·mL^{-1}), ILA + Cur + US (1.5 W·cm^{-2}, 1 MHz, 50% duty cycle, 3 min) , ILA + Cur@HMON@gel (containing Cur with a concentration of 1 mg·mL^{-1})、 ILA + Cur@HMON@gel + US (1.5 W·cm^{-2}, 1 MHz, 50% duty cycle, 3 min). The ILA treatment was performed using a diode laser system (SoracteLite, EchoLaser X4 system, Esaote, Italy) under the direction of a real-time ultrasonic unit with a multifrequency linear transducer (4–13 MHz, MyLab Twice, Esaote). After the procedure of ILA, 3D-CEUS was administrated to verify the
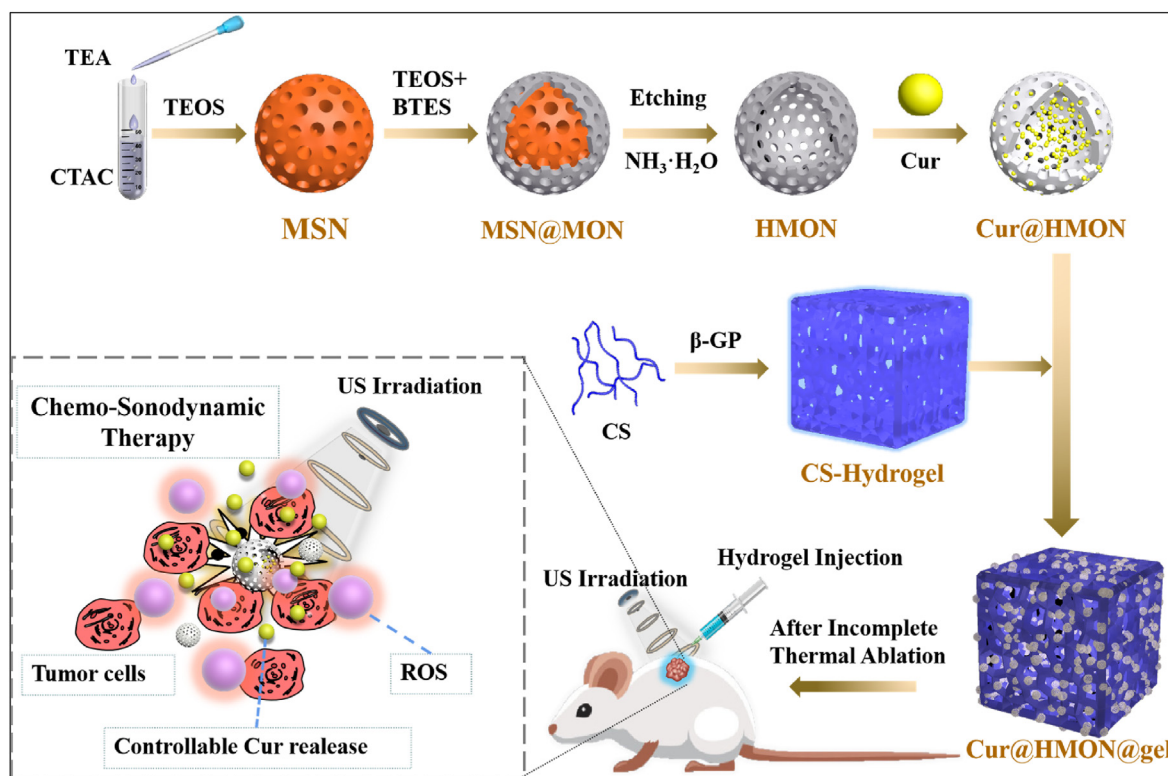
Fig. 1. Schematic illustration of the construction of chemo-sonodynamic therapeutic Cur@HMON@gel and its controlled Cur release and SDT against residual carcinoma after incomplete TA.

activity of residual tumor by observing tumor blood perfusion after the bolus injection of contrast medium (SonoVue, Bracco, Milan, Italy; 100 µL). After 24 h of ILA procedure, 100 µL of Cur solution or Cur@H-MON@gel containing 100 µg Cur was injected into the residual tumor under the guidance of ultrasound. US irradiation was conducted at 1.5 W·cm^{-2} for 3 min (1 min per cycle for each mouse in turn, 3 cycles) at 30 min after injection and every three days. The body weight of mice was recorded and 3D-CEUS examination was performed accordingly. The volume of the whole tumor or the enhanced part of residuals were measured using the quantitative image processing system in Aplio500 ultrasonic apparatus, and the volume enhanced residuals (V1) were then normalized to the initial volume after ILA was administrated (V0). After all mice were sacrificed at the end of experiment, subcutaneous tumor was isolated and sectioned into slices with H&E staining for histological observation. And the immunohistochemical analysis, including Rabbit monoclonal antibody against human proliferating nuclear antigen (Ki-67) and Cysteine aspartic acid proteinase 3 (Capase-3), were also performed to measure the proliferation and apoptotic properties of tumors. To further assess the therapeutic biosafety of Cur@HMON@gel with or without US irradiation, the H&E staining of the main organs (heart, kidney, liver, spleen, lung, and skin tissue adjacent to tumor site) of mice in ILA + Cur@HMON@gel and ILA + Cur@HMON@gel + US groups were obtained and analyzed at the end of research.

3. Results and discussion

3.1. Design, synthesis, and characterization of Cur@HMON@gel

Bearing the distinct advantage of antitumor and sonosensitive traits combined [21], Cur was chosen as a desirable therapeutic agent, in this work, to mop up the residual RCC after incomplete TA upon US irradiation. To improve the drug-delivery efficiency and tumor-accumulation capacity, Cur was encapsulated into the hollow interiors of HMON, and Cur-loaded HMON was then embedded in the thermosensitive hydrogel

to obtain the therapeutic Cur@HMON@gel biomaterial platform. Typically, HMON was synthesized by the structural difference-based alkaline etching strategy (Fig. 1). Briefly, a thin organic-inorganic hybrid mesoporous organosilica shell was deposited on the pure inner mesoporous silica nanoparticle (MSN) core, which was then selectively etched away in a hot ammonia solution. With a huge hollow interior and thioether-bridged framework, HMON enabled substantial encapsulation of Cur with two benzene molecules *via* the interaction of π-π supermolecular and hydrophobic-hydrophobic staking. Finally, in order to construct an injectable therapeutic biomaterial, Cur@HMON was embedded into the thermosensitive hydrogel matrix composed of CS and β-GP (Cur@HMON@gel), which showed a rapid phase transition at body temperature. Tracking by 3D-CEUS, the tumor growth of the mice received incomplete TA and Cur@HMON@gel injection was markedly suppressed with the assistance of sustained Cur release and ROS production upon US irradiation.

The representative spherical MSN@MON with narrow particle-size distribution can be observed from transmission electron microscope (TEM) image (Fig. 2a). The hollow interior structure of HMON was obtained by selectively etching of the MSN core (Fig. 2b). After the Cur loading, no obvious change can be observed in the spherical morphology and well-defined hollow nanostructure of HMON (Fig. 2c), and the representative elements are homogeneously distributed on its shell (Fig. S1). Especially, the well-designed mesoporous structure can also be confirmed by the high-resolution scanning electron microscope (SEM) images (Fig. 2d–f). Both prominent signals derived from Q and T silicon sites shown in ^{29}Si magic-angle spinning (MAS) solid-state NMR spectrum of HMON demonstrated the high cross-linking degree of the bissilylated precursors (Fig. 2g). Correspondingly, the signals at −56.1, −66.2, −90 and −120 ppm can be assigned to the characteristic resonances of (SiO)$_2$(OH)SiC (^{2}T, $\delta = -56.1$ ppm), (SiO)$_3$SiC (^{3}T, $\delta = -66.2$ ppm), (OH)Si(OSi)$_3$ (^{3}Q, $\delta = -90$ ppm) and Si(OSi)$_4$ (^{4}Q, $\delta = -120$ ppm), respectively. Additionally, the characteristic ^{1}C, ^{2}C, and ^{3}C carbon species of -Si-^{1}CH$_2^2$CH$_2^3$CH$_2$–S–S–S–^{3}CH$_2^2$CH$_2$–^{1}CH$_2$–Si- at 12.8, 22.3 and
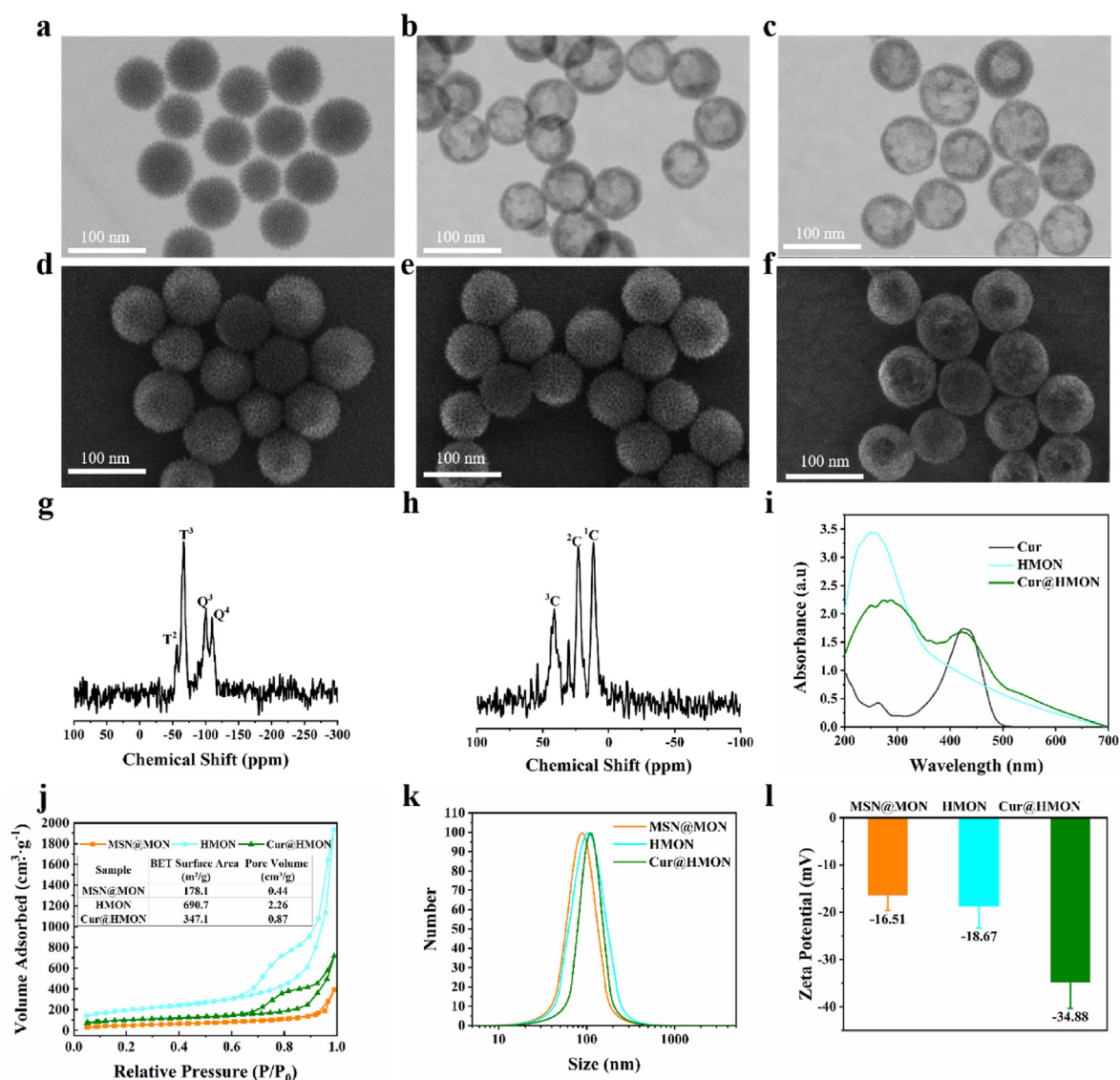
Fig. 2. Characterization of Cur@HMON. (a–c) Representative TEM images of (a) MSN@MON, (b) HMON, and (c) Cur@HMON. (d–f) Representative SEM images of (d) MSN@MON, (e) HMON, and (f) Cur@HMON, Scale bar = 100 nm. (g, h) Solid-state (g) ^{29}Si and (h) ^{13}C CPMAS NMR spectra of HMON. (i) UV–vis absorption spectra of Cur, HMON, and Cur@HMON. (j) N_2 adsorption-desorption isotherms, (k) particle-size distributions and (l) Zeta potential of MSN@MON, HMON, and Cur@HMON.

41.5 ppm were also present in the ^{13}C cross-polarization MAS (CPMAS) solid-state NMR spectrum (Fig. 2h), which further indicates the molecularly organic-inorganic hybrid framework of HMON.

To confirm the successful loading of Cur, the UV–vis absorption spectra and Fourier transform infrared spectroscopy (FTIR) analysis were conducted. Notably, a characteristic absorbance of Cur at 425 nm was detected in the UV–vis absorption spectra of Cur@HMON when comparing with HMON (Fig. 2i). Similarly, by comparing the FTIR spectra of HMON and Cur@HMON, the prominent absorption at 1580-1640 cm^{-1} was detected, which can be indexed as the characteristic stretching vibration of C=O in Cur (Fig. S2a). Furthermore, the obtained Cur@HMON shows a much lower Brunauer-Emmett-Teller (BET) surface area (347.1 m$^2 \cdot$g^{-1}) and pore volume (0.87 cm$^3 \cdot$g^{-1}) compared with HMON (690.7 m$^2 \cdot$g^{-1} and 2.26 cm$^3 \cdot$g^{-1}, respectively), which further demonstrates the efficient encapsulation of Cur (Fig. 2j). As expected, no obvious change was detected in the hydrodynamic diameters of MSN@MON, HMON, and Cur@HMON (Fig. 2k). Typically, the surface potential of MSN@MON was negative due to the exposure of abundant Si–OH group, and the subsequent core etching and Cur loading further

decreased the zeta potential of the nanoparticles (Fig. 2l). To calculate the drug encapsulation efficiency and loading capacity of HMON, the UV absorbance of Cur in the supernatant collected in the drug-loading process was detected. The Cur amount in supernatant solution was calculated to be 4.55 mg at a Cur/HMON feeding ratio of 0.2 (10 mg/50 mg), and the corresponding drug encapsulation efficiency and loading capacity of HMON were determined to be 45.5% and 8.34% using UV–vis spectroscopy, respectively (Fig. S2b).

To confine the Cur@HMON in tumor region, an CS/β-GP thermosensitive hydrogel was constructed. By the vial-inverting method, the sol-gel transfer behavior of hydrogel at specific temperature was demonstrated (Figs. S3a–c). The irregular microporous knot and internal framework of hydrogel made it possible to entrap nanoparticles in the interconnected pore and block them diffuse freely (Fig. S4). Additionally, with the increase of β-GP amount, the gelation time of CS/β-GP hydrogel under body temperature (37 °C) and the fluid absorbed by hydrogel were decreased gradually (Fig. 3a and b). In order to meet the requirement of rapid phase transformation and appreciable strength simultaneously, CS (2%)/β-GP (10%) hydrogel (gel) was selected for further investigation.
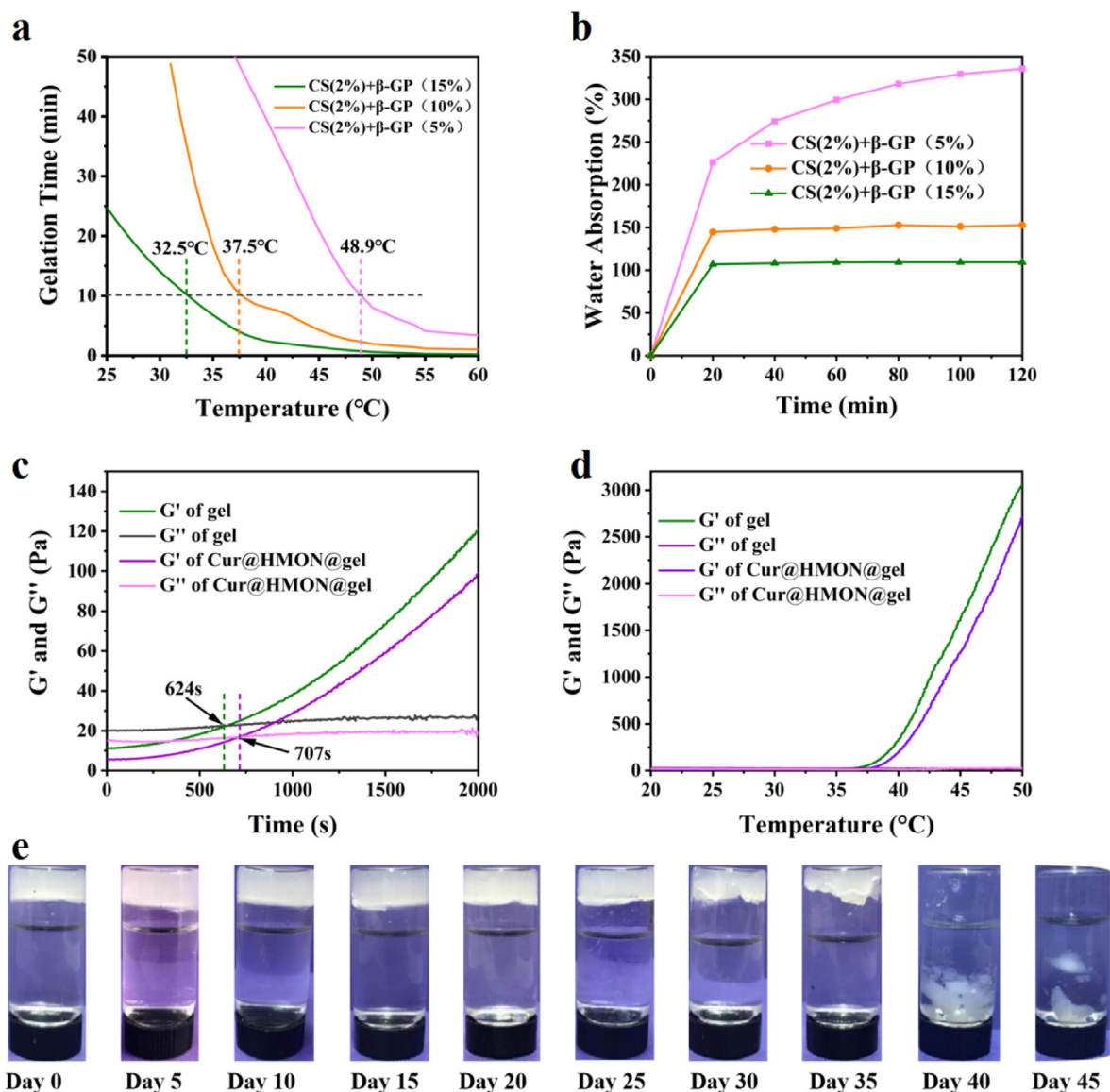
Fig. 3. Characteristics of CS/β-GP hydrogel. (a) Gelation time and (b) Water absorption behavior of series of CS/β-GP hydrogel with varied β-GP concentrations. (c) Time- and (d) temperature-dependences of the storage (*G′*) and loss (*G″*) modulus of blank CS/β-GP hydrogel and Cur@HMON@gel at 37 °C. (e) The degradation behavior of CS/β-GP hydrogel *in vitro*.

To verify the injectability of the blank thermogel (gel) and Cur@H-MON@gel in physiological environment (37 °C), the dynamic rheological measurements were performed, and their exact gelation time was determined to be 624 s and 707 s, respectively (Fig. 3c). The temperature dependence of the storage/loss modulus of the blank gel and Cur@H-MON@gel was also investigated and both of them demonstrated a transformation from liquid status to elastic gel phase below 37 °C (Fig. 3d). After immersing the gel-like matrix in the simulated body fluid at 37 °C, no obvious change was monitored for more than a month (Fig. 3e, Fig. S5), and there were only 26.38% of Cur@HMON@gel degraded after 30 days, which guarantees to confine the nanoparticles in tumor region and avoid adverse effects on normal tissues.

3.2. Controlled release of Cur and ROS generation upon US irradiation

To verify the on demand and controlled release behavior of Cur@HMON@gel upon US irradiation, UV absorbance of Cur at 425 nm was measured, which can be converted to the drug weight according to the standard curve mentioned above. As expected, almost all Cur drug

molecules packaged in the dialysis bag spontaneously diffuse to the medium in the first 2 h (96.8%). The release of Cur directly encapsulated in gel was slightly retained without burst release due to the diffusion barrier effect of gel, but the sustained release behavior cannot last for longer than 2 h, expelling the large proportion of confined Cur at early US irradiation time. By contrast, Cur loaded in HMON demonstrates a slow and sustained low-dose release pattern for 6 h (31.8%), while Cur in Cur@HMON@gel was well-confined in the matrix with negligible leakage (4.6%). Interestingly, under US irradiation, Cur in Cur@H-MON@gel demonstrated a pulsatile release pattern in the total six cycles (Fig. 4a), consistent with the therapeutic requirement that controlled and sustained drug release can be achieved upon external US triggering. The intriguing drug-releasing behavior is triggered by the mechanical/cavitation effect of US by breaking the interaction between Cur and organic-inorganic molecularly hybrid framework of HMON [41].

Simultaneously, as a sonosensitizer, the typical ESR technology was employed to verify the exact ROS generated in the SDT process upon US irradiation under different conditions (Fig. 4b). The typical 1:1:1 triple signal of the 2, 2, 6, 6-tetramethyl-1-piperidinyloxyl (TEMPO) free
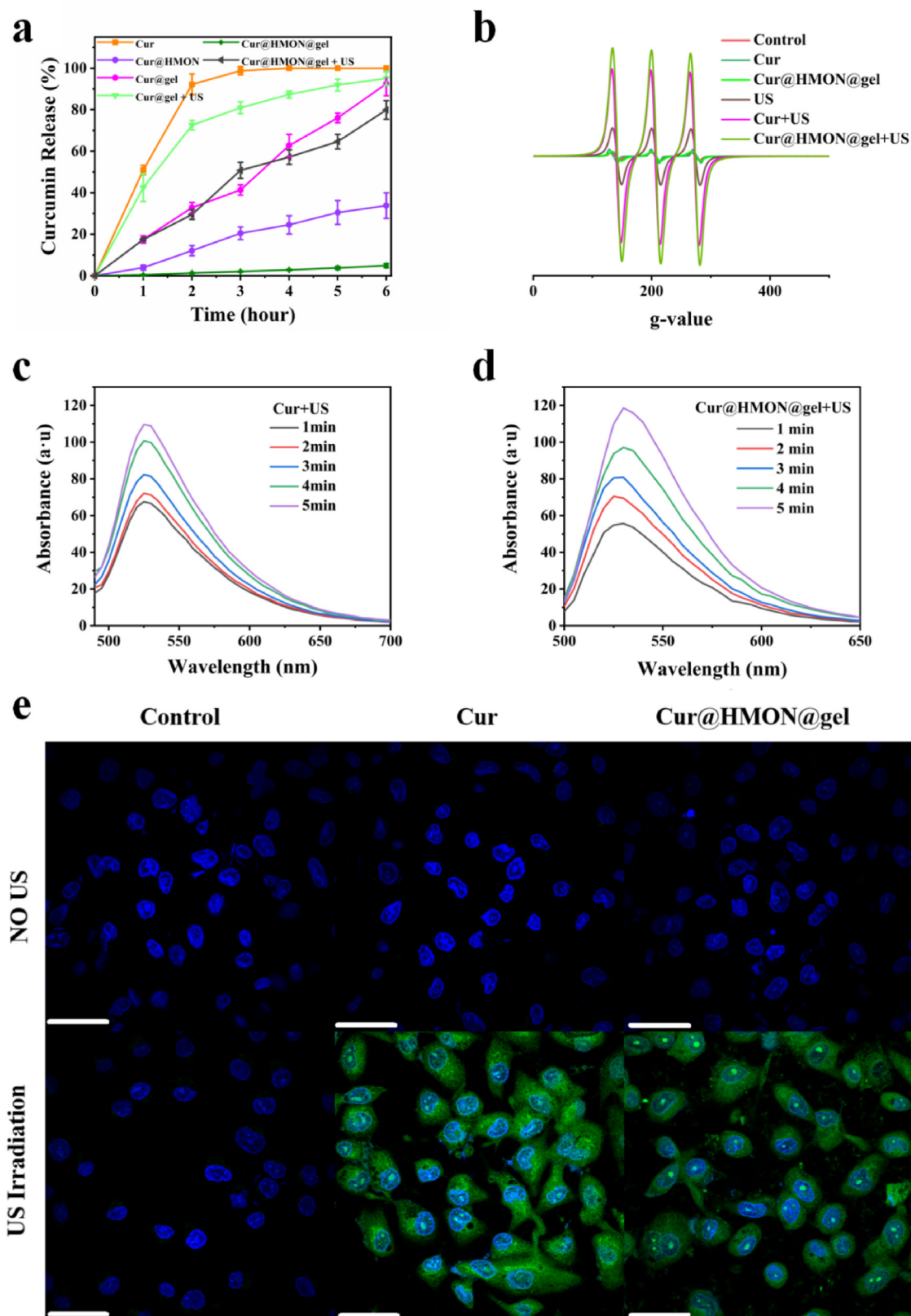
Fig. 4. Cur-releasing behavior and ROS-generation performance of Cur@HMON@gel under US irradiation. (a) *In vitro* Cur release profiles under different treatments, including Cur, Cur@HMON, Cur@gel and Cur@HMON@gel with or without US irradiation (1 MHz, 1.5 W·cm^{-2}, 50% duty cycle, 1 min). (b) Electron spin resonance (ESR) spectra of $^1O_2$ under different conditions, including Cur and Cur@HMON@gel with or without US irradiation (1 MHz, 1.5 W·cm^{-2}, 50% duty cycle, 1 min). (c, d) Fluorescence changes of SOSG ($\lambda_{ex} = 488$ nm, $\lambda_{em} = 525$ nm) in the presence of (c) naked Cur and (d) Cur@HMON@gel under US irradiation of varied durations. (e) Confocal laser scanning microscopy (CLSM) observation of RCC cells under different treatments, including Cur and Cur@HMON@gel with or without US irradiation (1 MHz, 1.5 W·cm^{-2}, 50% duty cycle, 1 min), (Scale bar = 40 μm).
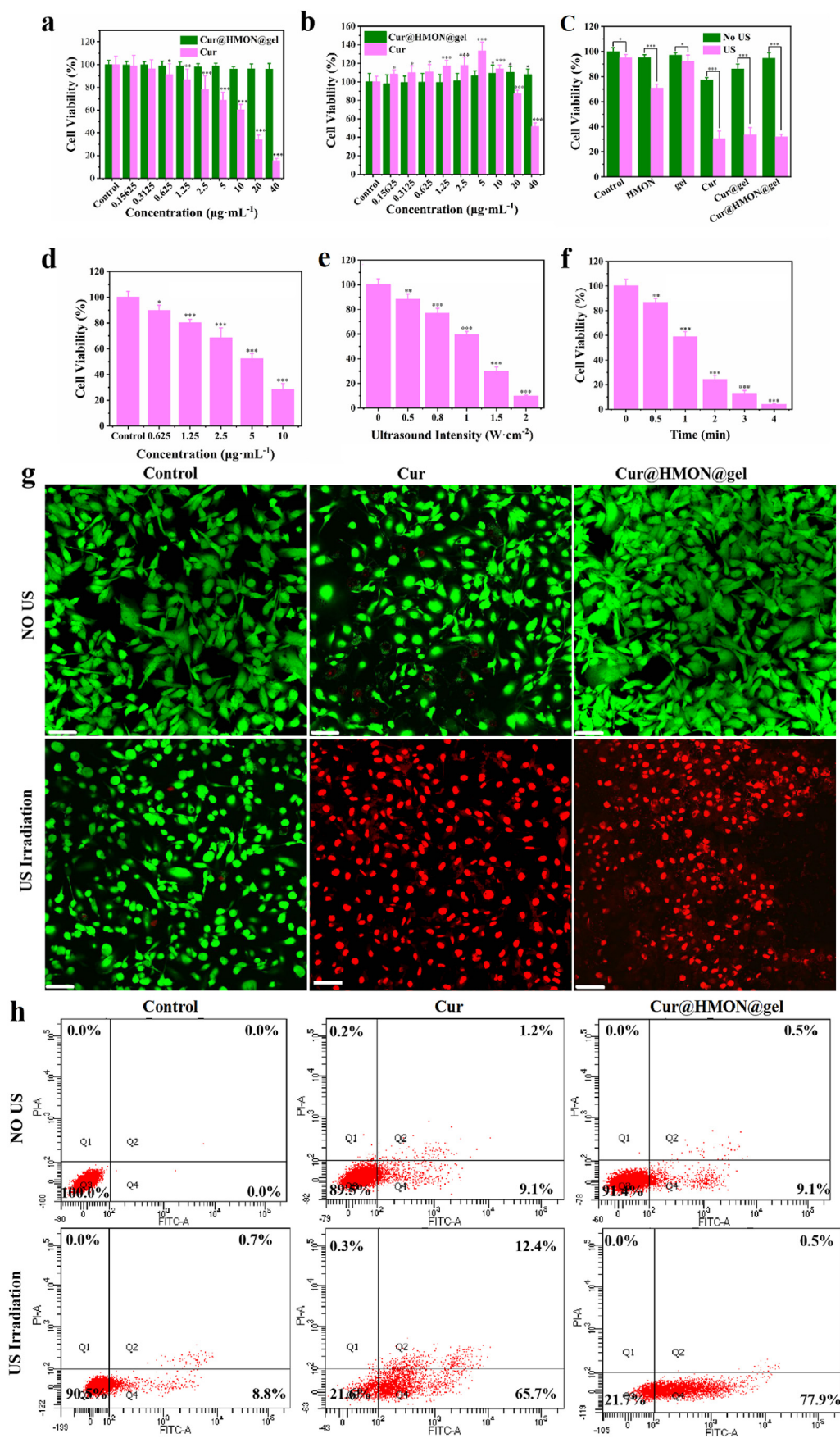
Fig. 5. *In vitro* **chemo-sonodynamic therapeutic efficacy of Cur and Cur@HMON@gel against 786-O cells.** (a, b) Cell viabilities of (a) 786-O cancer cells and (b) HUVECs after incubation with Cur and Cur@HMON@gel at gradient concentrations. (c) Cell viabilities of 786-O cells after different treatments (including control, Cur, HMON, gel and Cur@HMON@gel groups) with or without US irradiation (US power density = 1.5 W·cm^{-2}, US irradiation duration = 1.5 min). (d–f) Cell viabilities of 786-O cells treated with chemo-sonodynamic therapy under varied (d) Cur concentrations (US intensity = 1.5 W·cm^2, US time = 1.5 min), (e) US power densities (Cur concentration = 10 µg·mL^{-1}, US time = 1.5 min), and (f) US irradiation durations (US intensity = 1.5 W·cm^{-2}, Cur concentration = 10 µg·mL^{-1}). (n = 6, *$p < 0.05$, **$p < 0.01$, and ***$p < 0.001$.). (g) CLSM observation and (h) flow cytometry analysis of 786-O cells after various treatments, including control, Cur, Cur@HMON@gel, US only, Cur + US, and Cur@HMON@gel + US groups. Scale bar = 40 µm.

radical derived from conventional spin-trapping agent (2, 2, 6, 6-tetramethylpiperidine, TEMP) is suggested to determine the generation of single oxygen ($^1O_2$) [42,55]. Evidently, negligible signals of $^1O_2$ can be detected among groups with sensitizer- or US-triggering only, indicating that neither is dispensable. Significantly, prominent signal intensity of $^1O_2$ was observed in the Cur + US and Cur@HMON@gel + US group, due to the formation of excited species under the specific sonoluminescence mechanism. Subsequently, singlet oxygen sensor green (SOSG) reagent, a specific probe for $^1O_2$ [43], was applied to further semi-quantitatively verify the $^1O_2$ production (Fig. 4c and d). Though both of Cur@HMON@gel and Cur group clearly showed the dramatic increase in the fluorescence intensity under prolonged US irradiation, faster decline was achieved in Cur@HMON@gel group compared with Cur group. It is speculated that Cur is a special sonosensitizer with photosensitive traits [44,45], and unavoidable photolysis occurred in the experimental process, resulting in a low availability of naked drug Cur.

Furthermore, the intracellular $^1O_2$ generation was also verified by using 2′, 7′-dichlorofluorodiacetate (DCFH-DA), a cell-permeable probe to detect ROS, which can be converted to the fluorescent 2′,7′-dichlorofluorescein (DCF) by ROS oxidation [37,46,47]. Consistent with the *in vitro* ESR measurement, no obvious green fluorescence was observed inside RCC cell (human renal clear cell carcinoma cell, 786-O cell line) in all groups without US exposure, while significant DCF signal can be detected in both Cur + US (101.34 ± 35.85 au) and Cur@HMON@gel + US (89.03 ± 27.07 au) groups by CLSM observation (Fig. 4e), further demonstrating the US-triggered ROS production. Especially, the moderately weaker DCF fluorescence in Cur@HMON@gel + US group than Cur + US group was due to the burst exposure of all sensitizers upon US irradiation in free drug group but a sustained and controlled release of Cur upon US irradiation in Cur@HMON@gel group, which is consistent with the design for simultaneous pulsatile release of drug and ROS generation.

3.3. *In vitro chemo-sonodynamic therapy efficacy against cancer cells*

As a hydrophobic agent, the cytotoxicity of Cur was investigated in the aid of cosolvent dimethyl sulfoxide (DMSO) at a safe concentration (0.01% in this work, Fig. S6) by employing the standard cell-counting kit 8 (CCK-8) assay. Initially, the cell viability of 786-O cell was obviously inhibited by the naked drug Cur in a dose-dependent manner (Fig. 5a).

When it comes to human umbilical vein endothelial cells (HUVECs), low concentrations of Cur showed a cytoprotective action, while higher concentrations (more than 20 μg·mL^{-1}) were demonstrated to profoundly inhibit the proliferation (Fig. 5b), which was consistent with previous report [21,48]. Therefore, on demand and controlled Cur release is highly required for killing cancer cells to avoiding drug tolerance, in the meantime, protecting normal tissue from the side effect of Cur.

By embedding Cur-loaded HMON into thermogel, the nanoparticles are well-confined in the framework without obvious leakage. After co-incubation with these two cell lines (786-O and HUVECs), no significant inhibitory effect was observed even at the lethal concentration (Fig. 5a and b). The biocompatible and biosafe carrier and matrix showed negligible inhibition to cancer cell proliferation, while the cell viability of the naked drug group only remained 77% left. Under US irradiation, the cell viability of Cur-containing groups decreased sharply (Fig. 5c) to the same level, which demonstrates that the meticulously designed strategy could achieve an efficient tumor cell-killing efficiency and simultaneously circumvent the limitation of naked drug *via* controlled release of Cur and ROS generation. Especially, such a suppressive effect by Cur@HMON@gel combined with US exposure presented the specific Cur concentration-, US power intensity-, and US irradiation duration-dependent manner (Fig. 5d–f) [41,49,50].

Furthermore, to intuitively determine the chemo-sonodynamic therapeutic efficacy of Cur@HMON@gel combined with US triggering, both CLSM observation and flow cytometry analysis were conducted (Fig. 5g and h). In consistence with the ROS generation result, no obvious cell death was observed in all groups without US exposure, while significant cancer cell death could be detected both in Cur + US and Cur@HMON@gel + US groups.

3.4. *In vivo chemo-sonodynamic therapy in eliminating residual tumor after incomplete TA*

The on-demand and controlled Cur-releasing behavior and ROS generation efficacy of the constructed Cur@HMON@gel combined with US exposure provide highly promising potential for unavoidable residual RCC tumor elimination after incomplete TA. Initially, the *in vivo* biocompatibility evaluation of CS/β-GP hydrogel was comprehensively conducted on healthy male Kunming mice. There was no significant
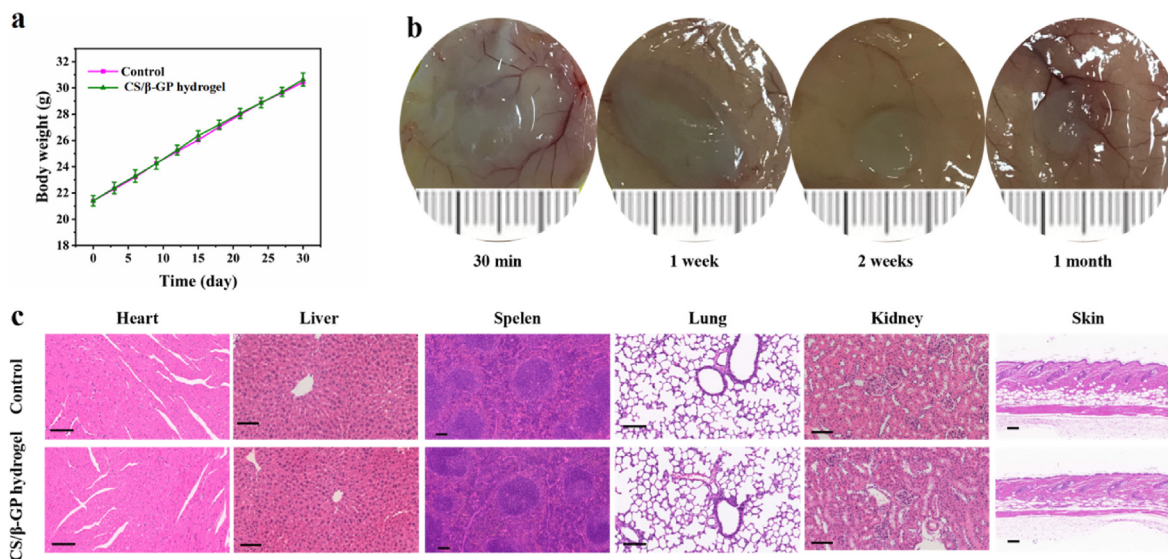
Fig. 6. ***In vitro* bio-capability of CS/β-GP hydrogel.** (a) The one-month weight growth curves of mice post-injected with CS/β-GP hydrogel. (b) The degradation behavior of CS/β-GP hydrogel *in vivo* (30 min, 1 week, 2 weeks and 1 month). (c) Histological slices obtained from heart, liver, spleen, lung, kidney and adjacent skin tissue of the treated mice at 30 days after injection of CS/β-GP hydrogel. Scale bar = 100 μm.
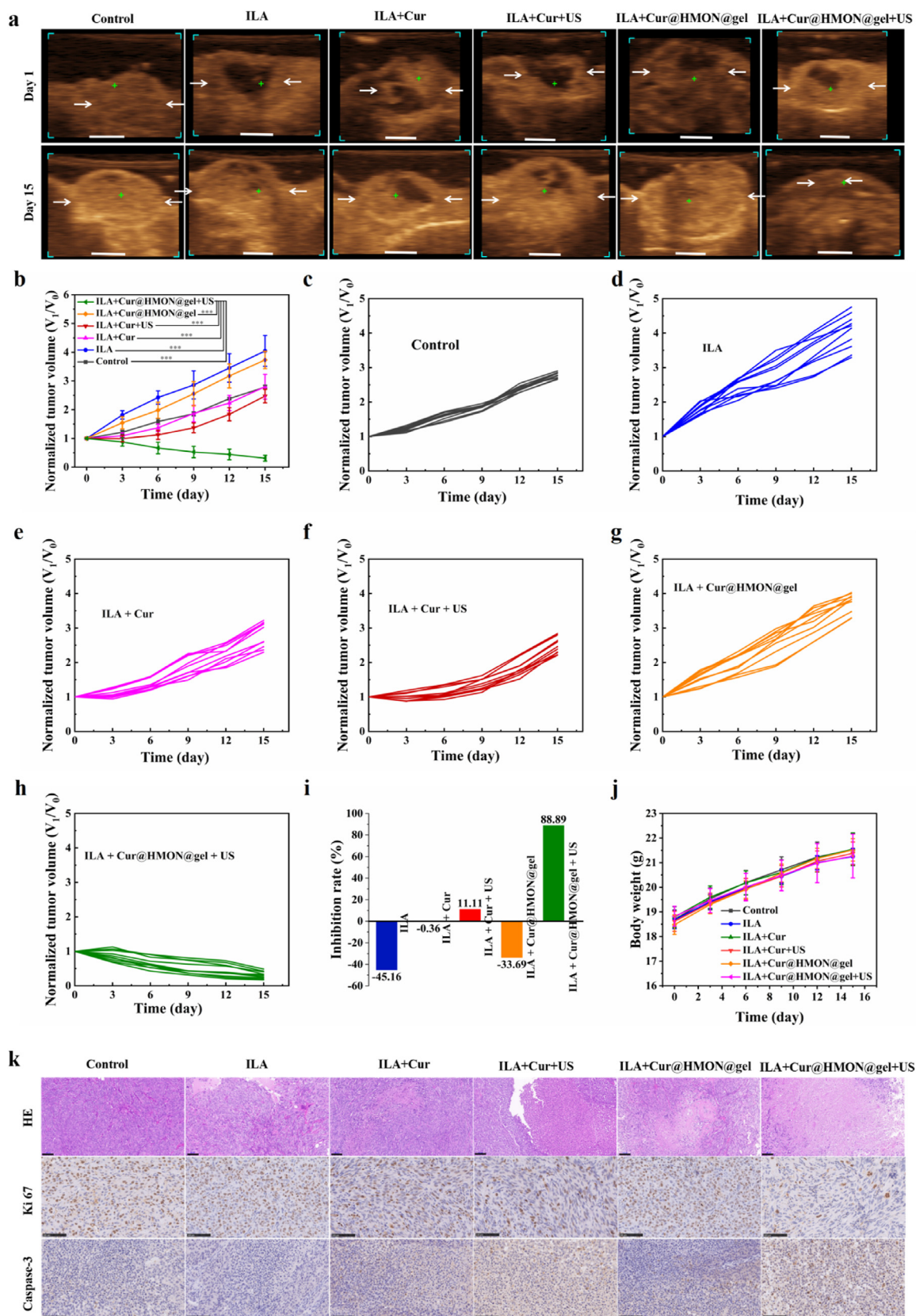
Fig. 7. *In vivo* **chemo-sonodynamic therapeutic efficacy of Cur@HMON@gel in eliminating residual RCC after ILA.** (a) The sagittal plane images of 3D-CEUS in each treatment group at the beginning and end of the experiment period (white arrow show the border of tumor). Scale bar = 2 mm. (b) The changes of normalized tumor volumes of the mice in each treatment group (*$p < 0.05$, **$p < 0.01$, and ***$p < 0.001$. Two independent sample *t*-test was used). (c–h) Individual tumor growth in volume (n = 10) (i) Tumor inhibition rate in each treatment group. (j) The changes of body weight of the mice during treatment. (k) H&E staining, antigen Ki67 and antigen Caspase-3 immunofluorescence staining of tumor sections from different groups. Scale bar = 100 μm.

body-weight loss observed after subcutaneous injection of hydrogel in the right flank of mice compared with the control group administrated with phosphate buffer solution (PBS) injection for one-month feeding (Fig. 6a). During the whole evaluation period, the CS/β-GP hydrogel sustainably maintained an elastic gel-like status, even though gradually degraded (Fig. 6b), which guarantees the high accumulation of Cur@HMON in tumor region and negligible impact on normal tissues. Furthermore, the hematoxylin and eosin (H&E)-stained histological sections of the main organs, including heart, liver, spleen, lung and kidney, and skin tissues adjacent to hydrogel revealed no detectable pathological signs at the end of evaluation (Fig. S7 and Fig. 6c), indicating that CS/β-GP hydrogel features a high biocompatibility and low systemic toxicity after *in vivo* administration.

Subsequently, to verify the chemo-sonodynamic therapeutic efficacy of Cur@HMON@gel combined with US irradiation on mopping up the residual tumor after ILA, the active tumor volume changes under different treatments were monitored by 3D-CEUS, which can display the viable tumor tissue in three-dimensional stereo form *via* visualizing blood perfusion situation of tumor (Fig. 7a–h). Sixty 786-O tumor bearing mice were divided into six groups, including control group, ILA group (ILA only), ILA + Cur group (intratumoral injection of Cur after ILA), ILA + Cur + US group (intratumoral injection of Cur followed by US irradiation after ILA), ILA + Cur@HMON@gel group (intratumoral injection of Cur@HMON@gel after ILA) and ILA + Cur@HMON@gel + US group (intratumoral injection of Cur@HMON@gel followed by US irradiation after ILA). It is shown that the active tumor volume of ILA only group increased sharply after treatment, which were even larger than that of the control group. This phenomenon is due to the transient hypoxia condition after thermal treatment, which unfortunately, may lead to the high expression of hypoxia-inducible factor 1 (HIF-1) and angiogenetic growth factor, resulting in the following rapid growth of residual tumors [51,52]. Although in ILA + Cur and ILA + Cur + US groups, the tumor growth were slightly inhibited by the burst diffusion of Cur and the generation of ROS upon US irradiation at the initial stage, the residuals kept their growth progress after the 3rd day of treatment. Comparatively, obvious intratumoral necrosis was observed in Cur@HMON@gel + US group, and the residual RCC growth was significantly inhibited with a tumor inhibition rate of 88.89% by chemo-sonodynamic therapy *via* on-demand high dose release of Cur and ROS generation (Fig. 7i and Fig. S8). On the contrary, the only injection of Cur@HMON@gel after ILA made no difference to tumor process, which implied that the Cur@HMON was well-confined in the gel matrix with no effective dosage leakage, thus avoiding the development of drug tolerance [53,54]. The body-weight of mice presented no significant difference in each group during the whole duration, and there was no obvious signs of damage and inflammatory lesions in the H&E staining of the main organs (heart, kidney, liver, spleen, lung, and skin tissue adjacent to tumor site) of mice in ILA + Cur@HMON@gel and ILA + Cur@HMON@gel + US groups, further indicating the high biosafety of the constructed chemo-sonodynamic therapeutic agent (Fig. 7j and Fig. S9).

To further understand the underlying biological mechanism of the chemo-sonodynamic therapeutic efficacy by Cur@HMON@gel upon US irradiation to eliminate residual RCC after incomplete TA, the tumor sections at the end point of treatment cycle were collected and stained by H&E, Cysteine aspartic acid proteinase 3 (Capase-3), and Rabbit monoclonal antibody against human proliferating nuclear antigen (Ki-67) antibody (Fig. 7k). As observed from the top-ranking images, there occurred characteristic necrosis phenomenon, such as collapsed cytoskeleton, chromatin condensation, nucleus disintegration and cell lysis, in all treatment groups due to ILA. Additionally, the larger amount of necrosis was captured in Capase-3 process in ILA + Cur@HMON@gel + US group (Fig. 7k, middle-ranking images). Correspondingly, the tumor cell proliferation was significantly inhibited in ILA + Cur@HMON@gel + US group when compared with other groups (Fig. 7k, down-ranking images), in consistent with the 3D-CEUS images, further suggesting the tumor eradication effect of Cur@HMON@gel upon US irradiation by

promoting apoptosis and inhibiting cell proliferation of residual RCC after ILA.

4. Conclusions

In summary, we have successfully developed an injectable thermosensitive chemo-sonodynamic biomaterial platform by embedding Cur-loaded HMON nanomedicine into biocompatible and biodegradable CS/β-GP hydrogel, which integrates the on-demand and controlled drug-releasing capability and ROS generation capacity together under the high tissue-penetrating US irradiation. The drug-releasing behavior is triggered by the mechanical/cavitation effect of US by breaking the interaction between Cur and organic-inorganic molecularly hybrid framework of HMON, and the ROS generation is activated by the sonoluminescence effect of US irradiation. Consequently, the high chemo-sonodynamic therapeutic efficacy can be achieved to mop up the residue RCC tumor after incomplete TA based on the high accumulation of Cur@HMON in tumor region confined by the biocompatible and biodegradable thermogel, which circumvents the risk of drug resistance from sustained low-dose drug release and the side effect on normal tissue, as well as the repeated administration of anti-tumor agents. Monitoring by the emerging 3D-CEUS, it is highly expected to visually track the tumor elimination process, which provides an alternative for rescuing the incomplete TA and mopping up malignant tumors.

Credit author statement

Cuixian Li: Conceptualization, Validation, Investigation, Writing original draft, Funding acquisition. **Piao Zhu:**.Conceptualization, Methodology, Investigation, Writing - review & editing. **Huijing Xiang:** Writing - review & editing. **Yunjie Jin, Beilei Lu, and Yujia Shen:** Methodology, Investigation. **Wenping Wang**: Supervision, Funding acquisition. **Beijian Huang:** Conceptualization, Validation, Supervision, Funding acquisition. **Yu Chen:** Conceptualization, Methodology, Supervision.

Declaration of competing interest

The authors declare that they have no known competing financial interests or personal relationships that could have appeared to influence the work reported in this paper.

Data availability

Data will be made available on request.

Acknowledgements

Appendix A. Supplementary data

Supplementary data to this article can be found online at https://doi.org/10.1016/j.mtbio.2022.100513.

References

[1] R.L. Siegel, K.D. Miller, H.E. Fuchs, A. Jemal, Cancer statistics, 2021, CA A Cancer J. Clin. 71 (2021) 7–33.

[2] M. Lazaro, B.P. Valderrama, C. Suarez, G. De-Velasco, C. Beato, I. Chirivella, A. Gonzalez-Del-Alba, et al., SEOM clinical guideline for treatment of kidney cancer (2019), Clin. Transl. Oncol. 22 (2020) 256–269.

[3] A. Bex, Sequencing therapy for advanced renal cancer, Lancet Oncol. 21 (2020) 9–11.

[4] P. Verhagen, E.R. Boeve, The European association of urology guideline on renal cell carcinoma (RCC) is not concise in its recommendation to perform partial nephrectomy in T1b RCC, Eur. Urol. 76 (2019) 132–133.

[5] J. Yu, X. Zhang, H. Liu, R. Zhang, X. Yu, Z. Cheng, Z. Han, et al., Percutaneous microwave ablation versus laparoscopic partial nephrectomy for cT1a renal cell carcinoma: a propensity-matched cohort study of 1955 patients, Radiology 294 (2020) 698–706.

[6] J.K. Heimbach, L.M. Kulik, R.S. Finn, C.B. Sirlin, M.M. Abecassis, L.R. Roberts, A.X. Zhu, et al., AASLD guidelines for the treatment of hepatocellular carcinoma, Hepatology 67 (2018) 358–380.

[7] L. Shi, J. Wang, N. Ding, Y. Zhang, Y. Zhu, S. Dong, X. Wang, et al., Inflammation induced by incomplete radiofrequency ablation accelerates tumor progression and hinders PD-1 immunotherapy, Nat. Commun. 10 (2019) 5421.

[8] J. Linxweiler, K. Junker, Extracellular vesicles in urological malignancies: an update, Nat. Rev. Urol. 17 (2020) 11–27.

[9] S. Patra, B. Pradhan, R. Nayak, C. Behera, L. Rout, M. Jena, T. Efferth, et al., Chemotherapeutic efficacy of curcumin and resveratrol against cancer: chemoprevention, chemoprotection, drug synergism and clinical pharmacokinetics, Semin. Cancer Biol. 73 (2021) 310–320.

[10] X. Pang, C. Xu, Y. Jiang, Q. Xiao, A.W. Leung, Natural products in the discovery of novel sonosensitizers, Pharmacol. Ther. 162 (2016) 144–151.

[11] D.P.V. Ruiz, L. Layos, E. Martinez-Balibrea, Curcumin: a therapeutic strategy for colorectal cancer? Semin. Cancer Biol. 73 (2021) 321–330.

[12] X. Zhao, J. Liu, J. Fan, H. Chao, X. Peng, Recent progress in photosensitizers for overcoming the challenges of photodynamic therapy: from molecular design to application, Chem. Soc. Rev. 50 (2021) 4185–4219.

[13] U. Chilakamarthi, L. Giribabu, Photodynamic therapy: past, present and future, Chem. Rec. 17 (2017) 775–802.

[14] R. Han, M. Zhao, Z. Wang, H. Liu, S. Zhu, L. Huang, Y. Wang, et al., Super-efficient in vivo two-photon photodynamic therapy with a gold nanocluster as a type I photosensitizer, ACS Nano 14 (2020) 9532–9544.

[15] D. Wang, D.B. Cheng, L. Ji, L.J. Niu, X.H. Zhang, Y. Cong, R.H. Cao, et al., Precise magnetic resonance imaging-guided sonodynamic therapy for drug-resistant bacterial deep infection, Biomaterials 264 (2021), 120386.

[16] S. Liang, X. Deng, P. Ma, Z. Cheng, J. Lin, Recent advances in nanomaterial-assisted combinational sonodynamic cancer therapy, Adv. Mater. 32 (2020), e2003214.

[17] D. Sun, X. Pang, Y. Cheng, J. Ming, S. Xiang, C. Zhang, P. Lv, et al., Ultrasound-switchable nanozyme augments sonodynamic therapy against multidrug-resistant bacterial infection, ACS Nano 14 (2020) 2063–2076.

[18] S. Son, J.H. Kim, X. Wang, C. Zhang, S.A. Yoon, J. Shin, A. Sharma, et al., Multifunctional sonosensitizers in sonodynamic cancer therapy, Chem. Soc. Rev. 49 (2020) 3244–3261.

[19] Y. Zhang, X. Zhang, H. Yang, L. Yu, Y. Xu, A. Sharma, P. Yin, et al., Advanced biotechnology-assisted precise sonodynamic therapy, Chem. Soc. Rev. 50 (2021) 11227–11248.

[20] A.L. Lopresti, The problem of curcumin and its bioavailability: could its gastrointestinal influence contribute to its overall health-enhancing effects? Adv. Nutr. 9 (2018) 41–50.

[21] X.Y. Xu, X. Meng, S. Li, R.Y. Gan, Y. Li, H.B. Li, Bioactivity, Health benefits, and related molecular mechanisms of curcumin: current progress, challenges, and perspectives, Nutrients 10 (2018).

[22] C. Kang, E. Jung, H. Hyeon, S. Seon, D. Lee, Acid-activatable polymeric curcumin nanoparticles as therapeutic agents for osteoarthritis, Nanomedicine 23 (2020), 102104.

[23] D. George, P.U. Maheswari, K. Begum, Chitosan-cellulose hydrogel conjugated with L-histidine and zinc oxide nanoparticles for sustained drug delivery: kinetics and in-vitro biological studies, Carbohydr. Polym. 236 (2020), 116101.

[24] F.N. Sorasitthiyanukarn, C. Muangnoi, P. Rojsitthisak, P. Rojsitthisak, Chitosan-alginate nanoparticles as effective oral carriers to improve the stability, bioavailability, and cytotoxicity of curcumin diethyl disuccinate, Carbohydr. Polym. 256 (2021), 117426.

[25] Y. Wang, D. Gao, Y. Liu, X. Guo, S. Chen, L. Zeng, J. Ma, et al., Immunogenic-cell-killing and immunosuppression-inhibiting nanomedicine, Bioact. Mater. 6 (2021) 1513–1527.

[26] L. Huang, J. Feng, W. Fan, W. Tang, X. Rong, W. Liao, Z. Wei, et al., Intelligent pore switch of hollow mesoporous organosilica nanoparticles for high contrast magnetic resonance imaging and tumor-specific chemotherapy, Nano Lett. 21 (2021) 9551–9559.

[27] W. Tang, W. Fan, Z. Wang, W. Zhang, S. Zhou, Y. Liu, Z. Yang, et al., Acidity/reducibility dual-responsive hollow mesoporous organosilica nanoplatforms for tumor-specific self-assembly and synergistic therapy, ACS Nano 12 (2018) 12269–12283.

[28] F. Gao, J. Wu, S. Niu, T. Sun, F. Li, Y. Bai, L. Jin, et al., Biodegradable, pH-sensitive hollow mesoporous organosilica nanoparticle (HMON) with controlled release of pirfenidone and ultrasound-target-microbubble-destruction (UTMD) for pancreatic cancer treatment, Theranostics 9 (2019) 6002–6018.

[29] A.M. Nazief, P.S. Hassaan, H.M. Khalifa, M.S. Sokar, A.H. El-Kamel, Lipid-based gliclazide nanoparticles for treatment of diabetes: formulation, pharmacokinetics, pharmacodynamics and subacute toxicity study, Int. J. Nanomed. 15 (2020) 1129–1148.

[30] M. Bialik, M. Kuras, M. Sobczak, E. Oledzka, Biodegradable synthetic polyesters in the technology of controlled dosage forms of antihypertensive drugs - the overview, Expet Opin. Drug Deliv. 16 (2019) 953–967.

[31] N. Vasan, J. Baselga, D.M. Hyman, A view on drug resistance in cancer, Nature 575 (2019) 299–309.

[32] C.D. DiNardo, I.S. Tiong, A. Quaglieri, S. MacRaild, S. Loghavi, F.C. Brown, R. Thijssen, et al., Molecular patterns of response and treatment failure after frontline venetoclax combinations in older patients with AML, Blood 135 (2020) 791–803.

[33] X. Gao, P. Zhu, L. Yu, L. Yang, Y. Chen, Ultrasound/acidity-triggered and nanoparticle-enabled analgesia, Adv Healthc Mater 8 (2019), 1801350.

[34] Z. Teng, W. Li, Y. Tang, A. Elzatahry, G. Lu, D. Zhao, Mesoporous organosilica hollow nanoparticles: synthesis and applications, Adv. Mater. 31 (2019), e1707612.

[35] Y. Xiao, T. Zhang, X. Ma, Q.C. Yang, L.L. Yang, S.C. Yang, M. Liang, et al., Microenvironment-responsive prodrug-induced pyroptosis boosts cancer immunotherapy, Adv. Sci. 8 (2021) e2101840.

[36] B. Liu, S. Liang, Z. Wang, Q. Sun, F. He, S. Gai, P. Yang, et al., A tumor-microenvironment-responsive nanocomposite for hydrogen sulfide gas and trimodal-enhanced enzyme dynamic therapy, Adv. Mater. 33 (2021), e2101223.

[37] X. Wang, B. Ma, J. Xue, J. Wu, J. Chang, C. Wu, Defective black nano-titania thermogels for cutaneous tumor-induced therapy and healing, Nano Lett. 19 (2019) 2138–2147.

[38] R. Zhang, Y. Li, M. Zhou, C. Wang, P. Feng, W. Miao, H. Huang, Photodynamic chitosan nano-assembly as a potent alternative candidate for combating antibiotic-resistant bacteria, ACS Appl. Mater. Interfaces 11 (2019) 26711–26721.

[39] Y. Du, Y. Qi, Z. Jin, J. Tian, Noninvasive imaging in cancer immunotherapy: the way to precision medicine, Cancer Lett. 466 (2019) 13–22.

[40] J.M. Llovet, R. Lencioni, mRECIST for HCC: performance and novel refinements, J. Hepatol. 72 (2020) 288–306.

[41] J. Lee, J.H. Kim, D.G. You, S. Kim, W. Um, J. Jeon, C.H. Kim, et al., Cavitation-inducible mesoporous silica-titania nanoparticles for cancer sonotheranostics, Adv. Healthc. Mater. 9 (2020), e2000877.

[42] Y. Chong, C. Ge, G. Fang, X. Tian, X. Ma, T. Wen, W.G. Wamer, et al., Crossover between anti- and pro-oxidant activities of graphene quantum dots in the absence or presence of light, ACS Nano 10 (2016) 8690–8699.

[43] W. Hou, Y. Yuan, Z. Sun, S. Guo, H. Dong, C. Wu, Ratiometric fluorescent detection of intracellular singlet oxygen by semiconducting polymer dots, Anal. Chem. 90 (2018) 14629–14634.

[44] V.B. Swami, P.S. Oh, S.H. Kim, H.J. Jeong, Curcuminoids encapsulated liposome nanoparticles as a blue light emitting diode induced photodynamic therapeutic system for cancer treatment, J. Photochem. Photobiol., B 205 (2020), 111840.

[45] S. Malekmohammadi, H. Hadadzadeh, S. Rezakhani, Z. Amirghofran, Design and synthesis of gatekeeper coated dendritic silica/titania mesoporous nanoparticles with sustained and controlled drug release properties for targeted synergetic chemo-sonodynamic therapy, ACS Biomater. Sci. Eng. 5 (2019) 4405–4415.

[46] L.R. Silveira, Critical and methodological analyses on the determination of oxygen and nitrogen reactive species in skeletal muscle cells during contractions, Arq. Bras. Endocrinol. Metabol. 48 (2004) 812–822.

[47] X. Han, J. Huang, X. Jing, D. Yang, H. Lin, Z. Wang, P. Li, et al., Oxygen-deficient black titania for synergistic/enhanced sonodynamic and photoinduced cancer therapy at near infrared-II biowindow, ACS Nano 12 (2018) 4545–4555.

[48] K. Khorsandi, R. Hosseinzadeh, F.K. Shahidi, Photodynamic treatment with anionic nanoclays containing curcumin on human triple-negative breast cancer cells: cellular and biochemical studies, J. Cell. Biochem. 120 (2019) 4998–5009.

[49] Y. Ding, Z. Song, Q. Liu, S. Wei, L. Zhou, J. Zhou, J. Shen, An enhanced chemotherapeutic effect facilitated by sonication of MSN, Dalton Trans. 46 (2017) 11875–11883.

[50] X. Pan, H. Wang, S. Wang, X. Sun, L. Wang, W. Wang, H. Shen, et al., Sonodynamic therapy (SDT): a novel strategy for cancer nanotheranostics, Sci. China Life Sci. 61 (2018) 415–426.

[51] J. Wan, X. Ling, Z. Rao, B. Peng, G. Ding, Independent prognostic value of HIF-1alpha expression in radiofrequency ablation of lung cancer, Oncol. Lett. 19 (2020) 849–857.

[52] Y. Luo, X. Teng, L. Zhang, J. Chen, Z. Liu, X. Chen, S. Zhao, et al., CD146-HIF-1alpha hypoxic reprogramming drives vascular remodeling and pulmonary arterial hypertension, Nat. Commun. 10 (2019) 3551.

[53] D. Mathur, B.P. Taylor, W.K. Chatila, H.I. Scher, N. Schultz, P. Razavi, J.B. Xavier, Optimal strategy and benefit of pulsed therapy depend on tumor heterogeneity and aggressiveness at time of treatment initiation, Mol. Cancer Therapeut. 21 (2022) 831–843.

[54] P. Davoodi, L.Y. Lee, Q. Xu, V. Sunil, Y. Sun, S. Soh, C.H. Wang, Drug delivery systems for programmed and on-demand release, Adv. Drug Deliv. Rev. 132 (2018) 104–138.

[55] P. Zhu, Y. Chen, J. Shi, Nanoenzyme-Augmented Cancer Sonodynamic Therapy by Catalytic Tumor Oxygenation, ACS Nano 12 (2018) 3780–3795.

[56] L. Li, Z. Yang, W. Fan, L. He, C. Cui, J. Zou, W. Tang, et al., In Situ Polymerized Hollow Mesoporous Organosilica Biocatalysis Nanoreactor for Enhancing ROS-Mediated Anticancer Therapy, Adv. Funct. Mater. 30 (2020) 1907716.